

Glass-like Thermal Conductivity in Higher Manganese Silicides with Grain Boundary Nanostructures

Youming Xu,¹ Shuchen Li,¹ Shucheng Guo,¹ Jianshi Zhou,² Li Shi,² Xi Chen^{1,*}

1.Department of Electrical and Computer Engineering, University of California, Riverside, CA, 92521, United States.

2.Department of Mechanical Engineering and Texas Materials Institute, The University of Texas at Austin, Austin, TX, 78712, United States.

* Corresponding author. Email: xichen@ucr.edu

Abstract

Higher manganese silicides (HMSs) have emerged as promising candidates for environmentally friendly thermoelectric (TE) materials due to their earth-abundant and non-toxic composition. We report grain boundary engineering in ruthenium-doped HMSs via a melt-quenching followed by annealing method. This approach induces formation of MnSi nanoprecipitates and nanopores, preferentially near grain boundaries. The presence of these nanostructures results in a weak temperature-dependent thermal conductivity, resembling glass-like thermal transport behavior. A two-channel model incorporating propagons and diffusons describes this glass-like thermal conductivity, with diffusons contributing about 60% of the lattice thermal conductivity at 300 K. Furthermore, the quench-annealing process enhances electrical conductivity while preserving a large Seebeck coefficient, which is attributed to a high density of states effective mass of $12 m_0$. As a result of improved power factor and reduced thermal conductivity, the figure of merit zT value increases by 33% at 300 K compared to undoped HMS synthesized via solid-state reaction. These findings present a promising strategy for manipulating phonon dynamics in functional materials and designing efficient thermoelectric systems.

Keywords: thermoelectrics, higher manganese silicides, melt-quenching, nanoprecipitates, nanopores, thermal transport

1 Introduction

Solid-state thermoelectric (TE) technology, which can directly convert temperature gradients into electricity and vice versa, allows waste heat recovery and refrigeration [1-4]. Without moving parts, TE

devices require little maintenance and can be readily integrated with other energy conversion devices [5, 6]. The energy efficiency of TE devices is limited by the dimensionless figure of merit $zT = S^2\sigma T/(\kappa_e + \kappa_L)$ of TE materials. In this equation, S represents the Seebeck coefficient, σ is the electrical conductivity, T represents the absolute temperature, κ_e is the electronic thermal conductivity, and κ_L is the lattice thermal conductivity. The product of $S^2\sigma$ is called power factor (PF). Currently, several strategies have been employed to enhance the performance of TE materials, including chemical doping,[7-10] nanostructuring [11-14], alloy scattering [15, 16], resonant energy level doping [17], convergence of electronic bands [18, 19], phonon engineering [20, 21], and the exploration of new materials [22, 23].

Environmentally friendly TE materials composed of earth-abundant and non-toxic elements have attracted growing interest recently [24-27]. Among these, higher manganese silicides (HMSs) stand out with promising TE performance for intermediate-temperature energy conversion. HMSs are p-type TE materials with Nowotny chimney ladder (NCL) phases, characterized by a tetragonal Mn sublattice (chimney) and a Si sublattice (ladder) [28, 29]. The periodicities of the two sublattices along the c -axis are usually incommensurate, where the compound can be expressed as MnSi_γ with a non-integer incommensurate c -axis ratio $\gamma = c_{\text{Mn}}/c_{\text{Si}}$. The crystal structures of several members in the HMS family, i.e. Mn_4Si_7 , $\text{Mn}_{11}\text{Si}_{19}$, $\text{Mn}_{15}\text{Si}_{25}$ and $\text{Mn}_{27}\text{Si}_{47}$, have been reported [28-31]. These phases have a similar a -axis but different c -axis ranging from 17.5 to 117.9 Å.

Recent advancements on HMSs have focused on reducing the thermal conductivity (κ) through heavy element substitution and nanostructuring while enhancing the PF via chemical doping [32-36]. Chen *et al.* [37] utilized inelastic neutron scattering measurements and first-principles calculations to investigate the phonon dispersions in HMS. They identified several low-energy optical phonon modes, including a distinctive polarization associated with the twisting of Si ladders inside the Mn chimneys. Scattering of acoustic phonons with this low-lying optical polarization contribute to the intrinsically low κ of HMS. Additionally, a two-channel model of both propagons and diffusons was proposed to explain their low and anisotropic thermal conductivity. Chen *et al.* [38] substituted Mn with the heavier element rhenium (Re) to enhance point defect scattering, resulting in a lattice thermal conductivity 30% lower than that of pure HMS at 723 K. Similarly, Zhou *et al.* [39] and Luo *et al.* [40] demonstrated that SiGe additions and Al doping, respectively, introduced defects that enhanced phonon scattering and suppressed the thermal conductivity. Additionally, Al doping improved the electrical conductivity by increasing the carrier concentration, which in turn enhanced the PF. Recently, Chauhan *et al.* [41] co-substituted V and Fe elements at the Mn sites in HMS, achieving charge compensation and enhancing lattice anharmonicity. The charge compensation led to an optimized charge carrier concentration and an improved PF, while the structural modulation-induced anharmonicity resulted in a reduced lattice thermal conductivity. Yu *et al.* [42] showed that the TE properties

of HMS are enhanced through isoelectronic anion and cation co-doping combined with embedded quantum dot techniques. The PF was improved due to band structure modification and charge transfer effects. Additionally, increased phonon scattering from point defects and nanoprecipitates significantly lowers lattice thermal conductivity, leading to an enhanced zT .

Beyond doping and nanostructuring, grain boundary engineering has emerged as an effective strategy for enhancing the performance of TE materials [43, 44]. Modified grain boundary structures can further suppress phonon thermal transport while maintaining electrical performance through the introduction of defects, such as segregated secondary phases, strain fields, pores, or dislocations [45-50]. In addition, the incorporation of secondary phases, such as metallic nanoparticles, at grain boundaries can induce a carrier filtering effect, which enhances the Seebeck coefficient by preferentially scattering low-energy carriers and effectively increasing the density-of-states (DOS) effective mass [51, 52]. Despite these advances, there is a lack of studies applying grain boundary engineering, particularly through in situ methods, to enhance the thermoelectric performance of HMS.

In this work, we investigate the TE properties of Ru-doped HMS with in situ formed nanostructures, prepared via melt-quenching followed by annealing. This method facilitates the formation of MnSi precipitates and pores with a wide size distribution near grain boundaries. The obtained sample shows a glass-like thermal conductivity, distinct from the samples prepared by solid-state reaction. A two-channel model incorporating contributions from propagons and diffusons is employed to understand this low thermal conductivity. Furthermore, quench-annealing process enhances electrical conductivity above 200 K while the Seebeck coefficient remains nearly unchanged due to the enhanced DOS effective mass. As a result, the quench-annealed sample demonstrates a 33% enhancement in zT at 300 K, owing to the enhanced PF and reduced lattice thermal conductivity. This study highlights the potential of grain boundary engineering for controlling heat conduction in thermoelectric materials.

2 Experimental

2.1 Preparation of HMSs

The starting materials are Mn (purity, 99.95%), Ru (purity, 99.9%) and Si (purity, 99.999%) powders. Three HMS samples were synthesized by either melt-quenching or solid-state reaction (SSR), followed by cold-pressing and annealing. For the melt-quenching synthesis, powders with a nominal chemical composition of $\text{Mn}_{0.95}\text{Ru}_{0.05}\text{Si}_{1.78}$ were weighed and hand-ground with an agate mortar and pestle for 1 hour. The powder was then sealed in an evacuated quartz tube and sintered at 900 °C for 30 hours to

obtain a pure phase. Next, the materials were melted at 1250 °C for 10 hours and quenched in water. The resulting ingot was ground into fine powder, cold-pressed under a maximum non-hydrostatic pressure of about 3 GPa [53], and then annealed at 1000 °C for 48 hours in a vacuum-sealed quartz tube. For comparison, undoped HMS ($\text{MnSi}_{1.78}$) and Ru-doped HMS ($\text{Mn}_{0.95}\text{Ru}_{0.05}\text{Si}_{1.78}$) were prepared by the SSR method at 900 °C for 48 hours in a vacuum. The obtained powders were cold pressed and annealed at 1100 °C for 15 hours in a vacuum-sealed quartz tube using a similar method.

2.2 Characterization of HMSs

The crystal structure of the samples was investigated by X-ray diffraction (XRD) with a Phillip X'pert diffractometer and the Cu $K\alpha$ radiation. The samples' morphology and chemical compositions were analyzed using a TESCAN Vega3 SBH scanning electron microscope (SEM) with an energy-dispersive X-ray (EDS) spectrometer. The density was measured by the Archimedes method. The resistivity was measured in the temperature range between 5 K and 823 K using the van der Pauw method on samples with a diameter of about 3 mm and a thickness of 0.2 mm. The Seebeck coefficient was measured in the temperature range 80-823 K with home-built setups. The thermal conductivity was measured using the steady-state method on rectangular specimens sized $0.5 \times 0.5 \times 2.5$ mm in the temperature range of approximately 5 K to 300 K [54, 55]. All three transport properties were measured along the direction perpendicular to the cold-pressing force. The Hall carrier concentration (p_H) and Hall mobility (μ_H) were measured using a Quantum Design physical property measurement system (PPMS) with a magnetic field sweeping between ± 2 T. The specific heat (C_p) of the samples from 2 to 300 K was also measured with the PPMS.

3. Results and discussion

3.1 Phase and Microstructures

Figure 1(a) shows the crystal structure of the simplest HMS phase, Mn_4Si_7 . The crystal structure consists of Mn sublattice forming the chimney and Si sublattice forming the ladder. Figure 1(b) shows the XRD patterns of Ru-doped HMS prepared by solid-state reaction and quench-annealing as well as undoped HMS prepared by solid-state reaction. All the samples are essentially single phase, which can be indexed as $\text{Mn}_{15}\text{Si}_{26}$ with space group $I\bar{4}2d$ (No. 122). A small amount of MnSi was detected in some samples. The zoomed-in view of the XRD patterns corresponding to $\{2\ 1\ 15\}$ planes is shown in Figure 1(c). A peak shift to the lower angle indicates the expansion of the lattice constants, which corresponds to lattice expansion

due to Ru doping with a larger atomic radius. For the quenched (QH) and quench-annealed (QA) Ru-HMS samples, the XRD analysis reveals notable changes before and after annealing. Prior to annealing, no MnSi phase is detected in the sample. However, after annealing, the emergence of MnSi is evident, accompanied by a shift in the XRD peaks to higher angles, as shown in Figure 1(c). This shift suggests a reduction in lattice constants (Figure 1(d)), indicating that the lattice contracts upon annealing. This contraction is likely due to the formation of MnSi, which depletes Mn from HMS matrix and subtly shrinking the lattice. In addition, it is noted that the lattice constants of the Ru-HMS-SSR and Ru-HMS-QA samples are nearly identical, suggesting a similar Ru concentration in the solid solution.

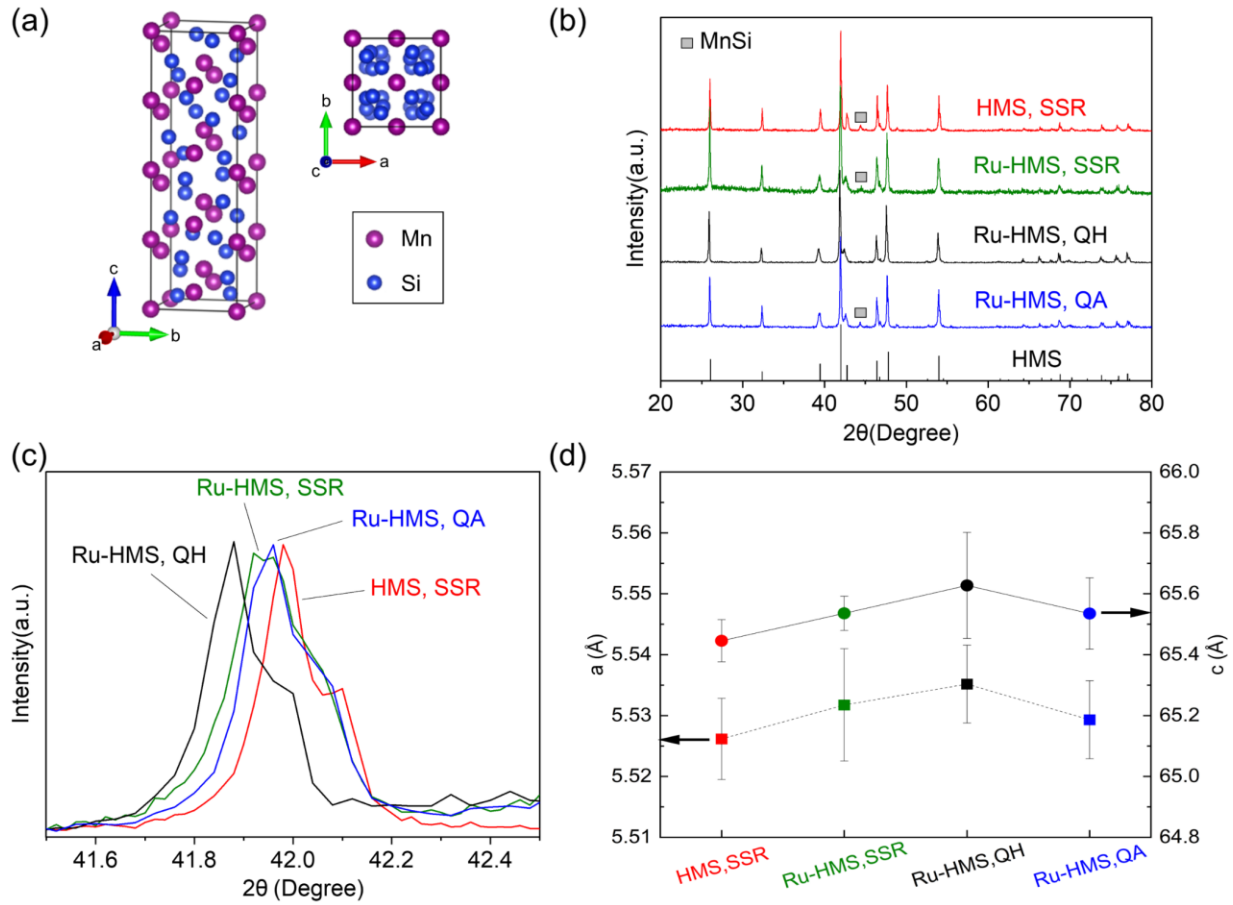


Figure 1. (a) Crystal structure of Mn_4Si_7 . (b) XRD patterns of various HMS samples. (c) Zoomed-in XRD pattern corresponding to $\{2\ 1\ 15\}$ plane for the HMS samples. (d) Lattice constants of HMS samples from fitting of XRD patterns.

Figure 2(a) and (b) show SEM images of the fractured surface of the Ru-doped HMS sample after quench-annealing. Some nanosized precipitates can be found on the surface of grains and exhibit an average

size of about 160 nm. Based on the XRD results, these nanoprecipitates can be attributed to the metallic phase MnSi. Furthermore, pores are clearly observed in the polished samples, as shown in Figure 2(c) and (d). Some of these pores are approximately 1-10 micrometers in size, while others are smaller, measuring around 50–300 nm. Additional SEM images can be found in the Supplementary Material. The calculated size distribution of nanopores is illustrated in Figure 2 (e). The pores have an average size of 290 nm. In contrast, such nanopores are not readily observed in the samples prepared by solid-state reaction followed by cold pressing [53]. Additionally, a few micrometer-sized secondary phases are visible in the sample, as indicated by the white arrows in Figure 2(f). EDS analysis indicates that the atomic ratio of Mn to Si in these secondary phases is approximately 1:1 (see Supplementary Material), consistent with the composition of MnSi. Figure 2(g–i) shows the EDS elemental maps of Mn, Si, and Ru. The mapping confirms that the secondary phases are enriched in Mn and deficient in Si relative to the matrix ($\text{MnSi}_{1.75}$), further supporting the formation of MnSi. These impurity phases are typically located near grain boundaries.

The formation of nanoprecipitates at grain boundaries has also been reported in other TE materials synthesized via non-equilibrium processing techniques, such as melt-spinning or melt-quenching followed by sintering or annealing [56, 57]. These processing methods often produce compositional inhomogeneities or metastable solid solutions that decompose upon subsequent heat treatment, resulting in secondary phase precipitation at energetically favorable sites such as grain boundaries [58]. In our study, MnSi nanoprecipitates formed at the grain boundaries as a result of slight Mn-rich deviation from the stoichiometric composition of HMSs. During annealing, the system enters a two-phase region in the Mn–Si phase diagram, where the HMS phase coexists with MnSi. Local Mn enrichment, particularly at grain boundaries due to segregation and enhanced diffusion, facilitates the nucleation and growth of MnSi precipitates at these interfaces. This precipitation process is also accompanied by the formation of nanopores near the grain boundaries. These pores likely originate from the Kirkendall effect [59], where unequal diffusion rates between Mn and Si during phase separation lead to vacancy supersaturation and eventual void formation. Additionally, the rejection of elements during precipitate formation and local volume contraction may further contribute to porosity. The concurrent presence of MnSi nanoprecipitates and nanopores at grain boundaries plays a critical role in electron and phonon transport in the material.

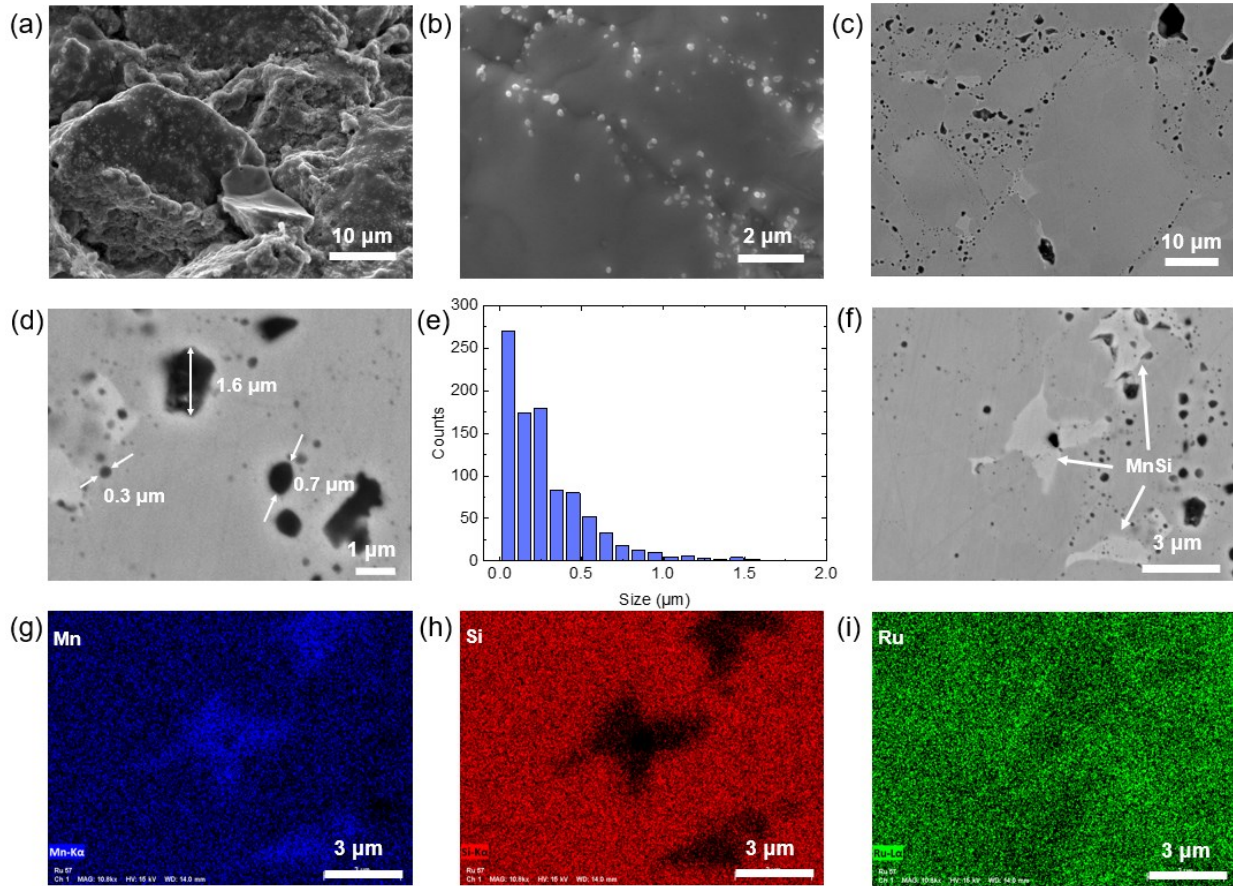


Figure 2. (a, b) SEM images of the fractured surface of the Ru-doped HMS sample after quench-annealing, showing the formation of nanoprecipitates. (c) SEM image of the polished surface revealing the presence of nanopores. (d) Magnified view highlighting both large and small pores. (e) Pore size distribution in the Ru-doped HMS sample, with an average size of 0.29 μm . (f-i) SEM image and corresponding EDS analysis of Mn, Si and Ru elements, showing MnSi secondary phases in the Ru-HMS sample after quench-annealing.

3.1 Electrical Properties

Ru atoms usually act as electron donors in the HMS when substituting for Mn atoms. Previous studies on Ru-doped HMS suggest that Ru negatively impacts TE performance of p-type HMS by reducing the electrical conductivity [60]. Figure 3(a) demonstrates the temperature dependence of the electrical conductivity of our samples. The n-type Ru substitution significantly decreases the electrical conductivity of p-type HMS at low temperatures. However, at higher temperatures as shown in Figure 3(b), the QA sample exhibits higher electrical conductivity than the other two samples. Figure 3(c) shows the temperature dependence of the Seebeck coefficient. All the samples exhibit the characteristics of p-type conduction. The

Seebeck coefficient gradually increases with temperature up to 750 K for all three samples. At low temperatures, the Seebeck coefficient increases linearly with temperature, which can be attributed to its degenerate semiconductor behavior [38, 61]. The Ru-doped samples exhibit an increased Seebeck coefficient in comparison to the undoped sample across almost the entire temperature range. Notably, the Ru-HMS-QA and Ru-HMS-SSR samples exhibit nearly identical Seebeck coefficients, while the QA sample shows higher electrical conductivity than the other. This improvement is likely due to improved crystallinity and reduced carrier scattering resulting from the melt-quench-anneal process. Furthermore, the formation of MnSi nanoprecipitates in the QA sample may contribute to an energy filtering effect at the interfaces between HMS and MnSi. Such an effect has been previously reported in HMS systems with embedded nanostructures, where the Seebeck coefficient is preserved or even enhanced despite an increase in carrier concentration [34, 42]. These combined mechanisms help explain the improved electrical performance observed in the QA sample.

The PF is shown in Figure 3(d). The quenched Ru-doped HMS achieves a peak PF of $1.62 \times 10^{-3} \text{ W m}^{-1} \text{ K}^{-2}$ at 756 K. In comparison, the maximum for the undoped HMS is only $1.15 \times 10^{-3} \text{ W m}^{-1} \text{ K}^{-2}$ at 726 K. In this work, we focus on comparing the thermoelectric properties of the SSR and QA samples to evaluate the influence of different synthesis methods. Because the QH sample represents an intermediate state, its thermoelectric properties were not characterized in this study and remain a subject for future investigation.

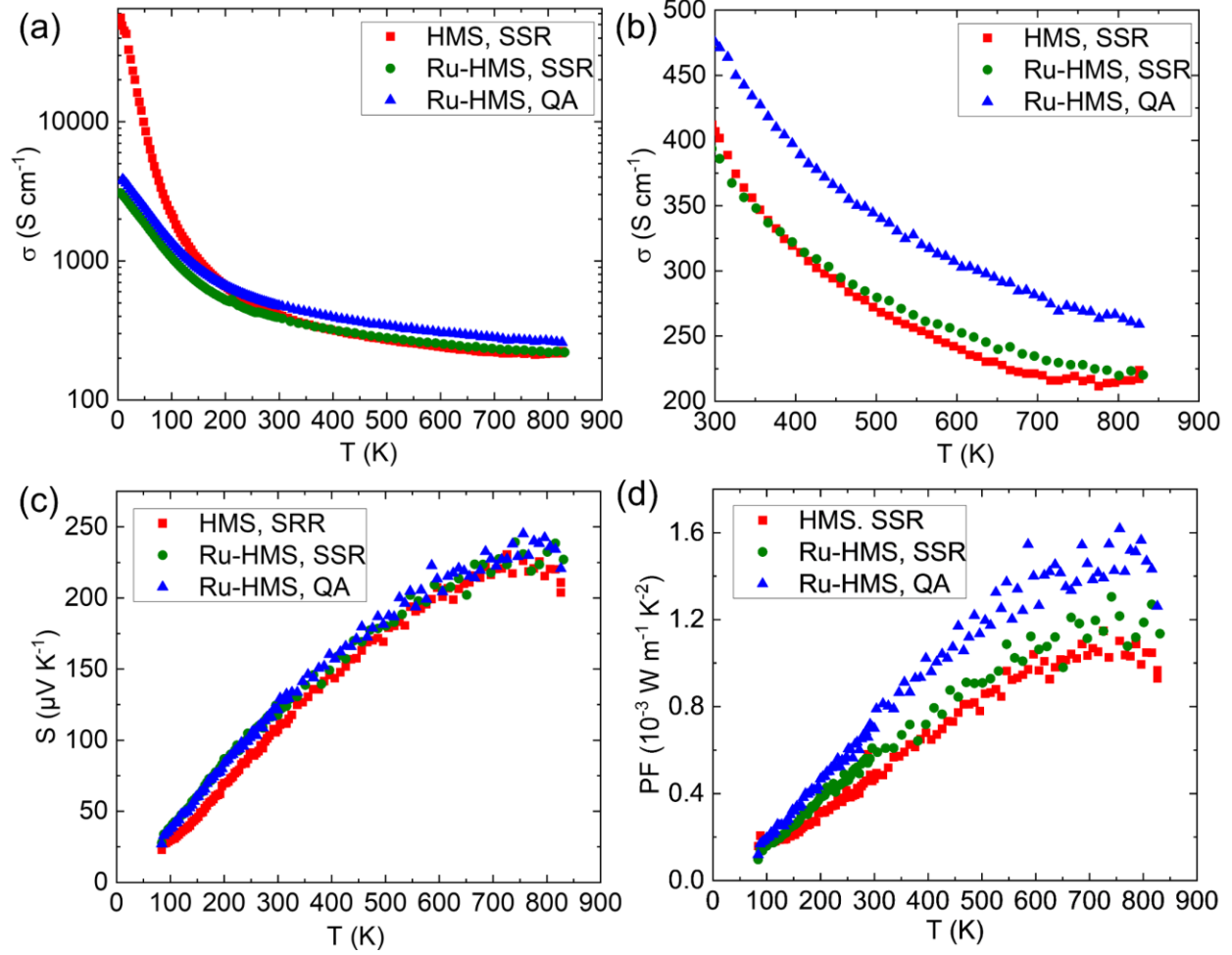


Figure 3. Temperature dependence of electrical properties for three HMS samples: (a) and (b) electrical conductivity with 5% uncertainty, (c) Seebeck coefficient with 5% uncertainty, (d) power factor with 11% uncertainty.

We further performed Hall effect measurement on the quench-annealed Ru-doped HMS. As shown in Figure 4(a), the hole concentration is nearly constant across the temperature range, which is characteristic of a degenerate p-type semiconductor [38, 61]. The room temperature carrier concentration is larger than that of the undoped HMS sample [62], possibly due to the formation of metallic MnSi phase or some p-type defects introduced during the quench-annealing process. Figure 4(b) presents mobility as a function of inverse temperature, following an approximately $T^{-3/2}$ dependence. This behavior is indicative of dominant acoustic phonon scattering in degenerate semiconductors at elevated temperatures [60]. The mobility values

range from approximately $10 \text{ cm}^2 \text{ V}^{-1} \text{ s}^{-1}$ at 20 K to about $1 \text{ cm}^2 \text{ V}^{-1} \text{ s}^{-1}$ at 300 K, which are lower than the undoped sample.

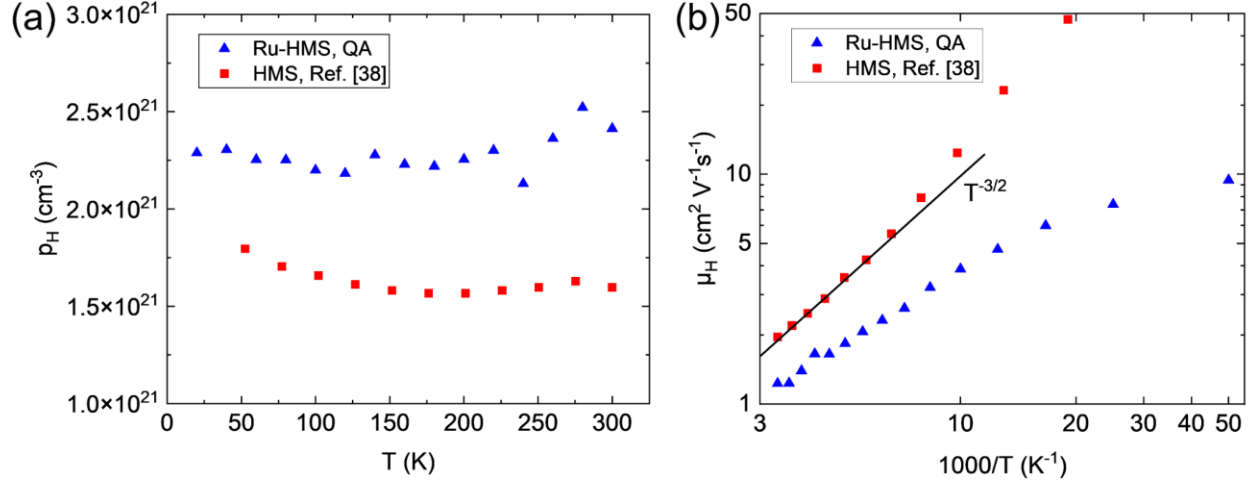


Figure 4. (a) Carrier concentration and (b) mobility of undoped HMS and quench-annealed Ru-HMS samples. The data for undoped HMS are taken from Ref. [38].

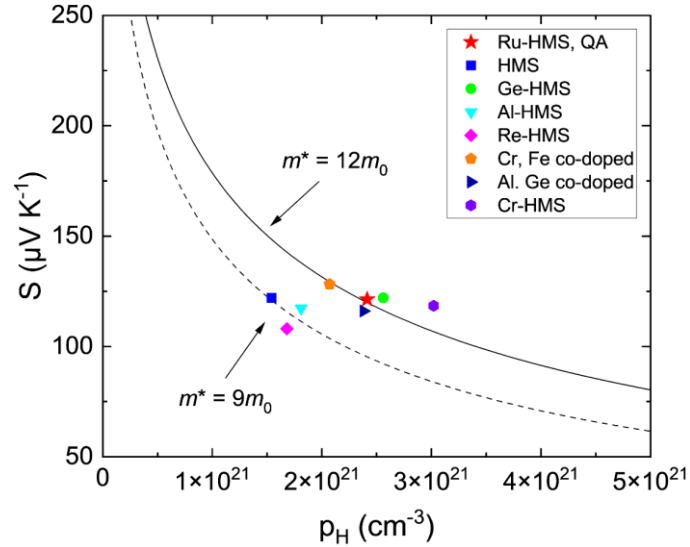


Figure 5. Seebeck coefficient as a function of carrier concentration p_H at 300 K. The effective mass for Ru-doped HMS is calculated to be $12 m_0$. The comparison to other doped HMS samples is also shown [38, 63-66].

To better understand the electrical properties of HMS, we used the measurement data to extract the DOS effective mass using a single parabolic band model [62]. The details of the calculation can be found

in the Supplementary Material. The relationship between the Seebeck coefficient and carrier concentration of quench-annealed Ru-HMS at 300 K is shown in Figure 5, alongside the data for other doped HMS samples [38, 63-66]. Our sample exhibits a higher carrier concentration than the undoped HMS while maintaining a comparable Seebeck coefficient, with an effective mass m^* of $12 m_0$ calculated using the single parabolic band model. This increased effective mass, likely resulting from the energy filtering effect, enables Ru-HMS to maintain a high Seebeck coefficient despite an increased carrier concentration.

3.3 Specific Heat and Thermal Conductivity

The specific heat data for the undoped and Ru-doped HMS samples are plotted in Figure 6(a). A previous study has reported that low-energy optical phonons and low-lying twisting modes contribute to the specific heat of HMS [37]. Accordingly, we employ a model that includes contributions from the electronic specific heat, a Debye term, and an Einstein term to fit the low-temperature specific heat data, using the following equation [67]:

$$\frac{C_p}{T^3} = \frac{\gamma}{T^2} + \frac{12\pi^4 N k_B}{5\theta_D^3} + n_E R \frac{\theta_E^2}{T^5} \frac{e^{\theta_E/T}}{(e^{\theta_E/T} - 1)^2}, \quad (1)$$

where γ is electronic specific heat coefficient, N is the number of atoms per mole, k_B is the Boltzmann constant, n_E is the Einstein oscillator strength per mole, and θ_D and θ_E are Debye and Einstein temperature, respectively. γ is proportional to the electron DOS at the Fermi level, which is proportional to the electron effective mass m^* , as shown in the following equation:

$$\gamma = \frac{\pi^2}{3} k_B^2 N(E_f) = 1.36 \times 10^{-4} \times V_{mol}^{\frac{2}{3}} n_\gamma^{\frac{1}{3}} \frac{m^*}{m_0}, \quad (2)$$

where V_{mol} is the molar volume and n_γ is the number of electrons per formula unit [19]. Figure 6 (b) and (c) shows C_p/T^3 as a function of T for undoped and Ru-doped HMS samples below 30 K. Although the Debye and Einstein contributions to the specific heat are nearly identical in the undoped and Ru-doped samples, the Ru-doped sample exhibits a higher electronic specific heat. The obtained electronic specific heat coefficient γ of the Ru-doped and undoped HMS are $7.81 \times 10^{-5} \text{ J g}^{-1} \text{ K}^{-2}$ ($8.38 \times 10^{-3} \text{ J mol}^{-1} \text{ K}^{-2}$) and $5.19 \times 10^{-5} \text{ J g}^{-1} \text{ K}^{-2}$ ($5.45 \times 10^{-3} \text{ J mol}^{-1} \text{ K}^{-2}$), respectively. This finding suggests a larger effective mass in the Ru-doped sample, consistent with our Seebeck coefficient analysis. The fitted Einstein temperatures for the undoped and Ru-doped HMS samples are 64 K and 61 K, respectively.

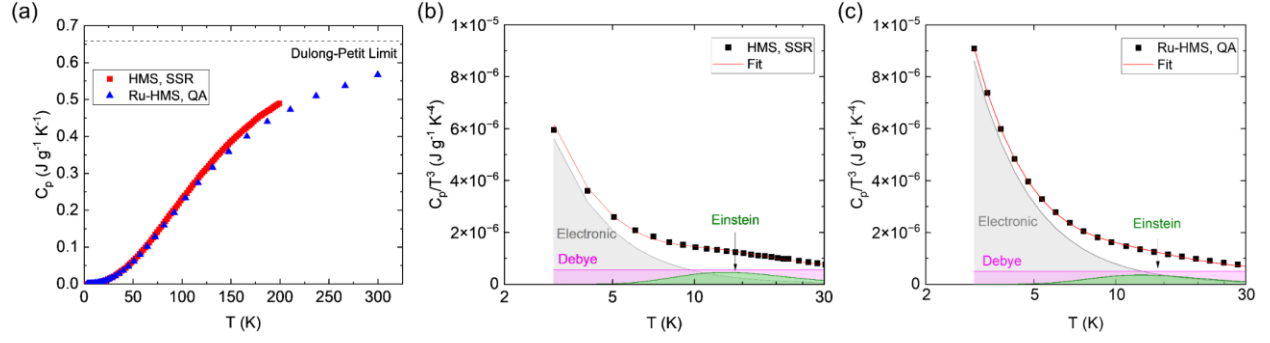


Figure 6. (a) Specific heat for undoped and Ru-doped HMS samples. C_p/T^3 as a function of temperature for (b) undoped and (c) Ru-doped HMS samples below 30 K. Specific heat contributions from electronic, Debye, and Einstein terms are labeled in gray, magenta, and green, respectively.

Figure 7(a) shows the measured thermal conductivity of the polycrystalline samples, which are compared with an HMS single crystal [37]. The low-temperature κ peak is largely suppressed in the polycrystal samples. Figure 7(b) shows the thermal conductivities of three samples plotted in linear scale. The total thermal conductivity of the Ru-doped sample is significantly reduced compared to the undoped sample, particularly within the temperature range of 6-100 K. This reduction is further enhanced in the quench-annealed sample.

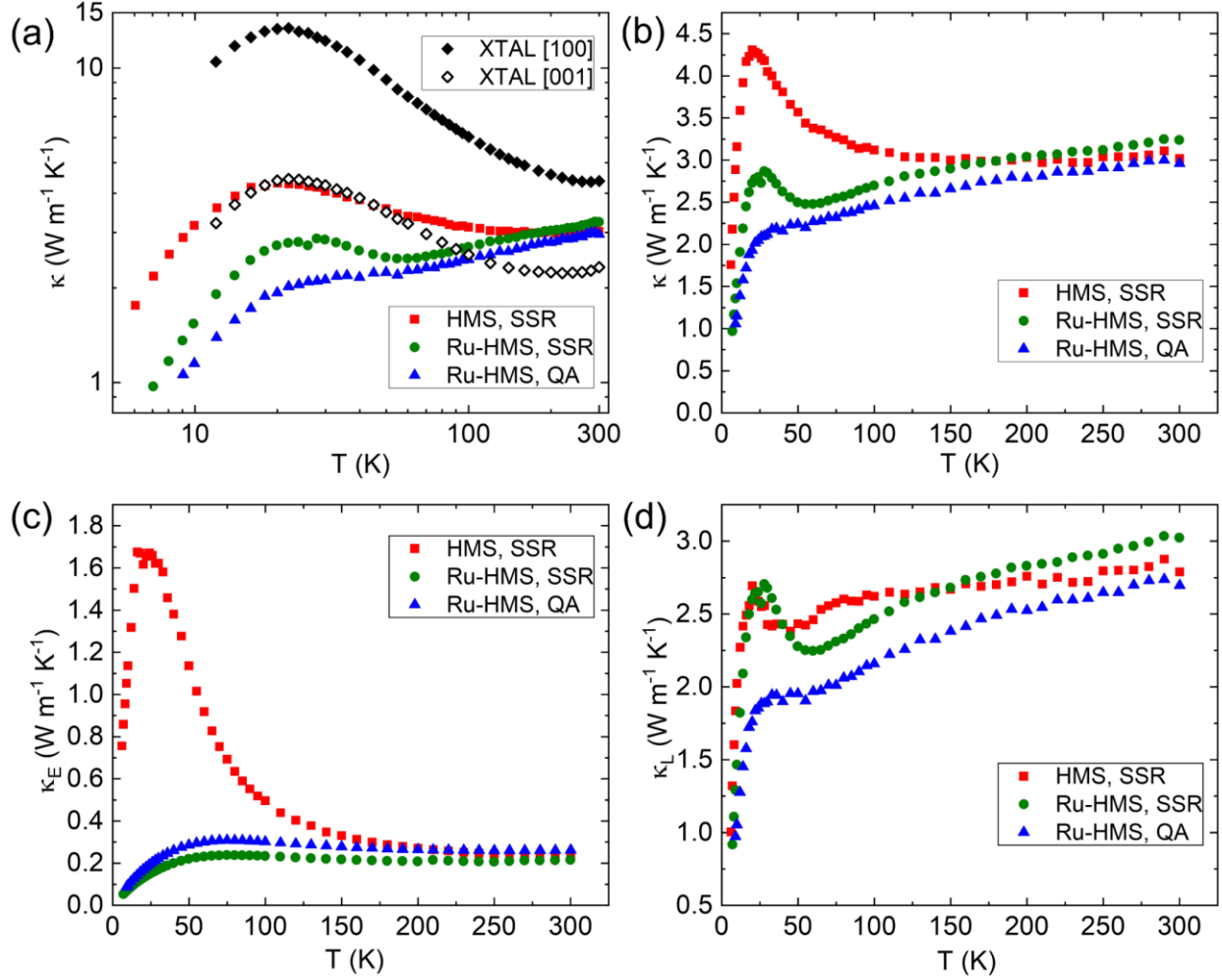


Figure 7. (a) Measured total thermal conductivities of three HMS samples with 10% uncertainty in comparison with the thermal conductivities of an HMS single crystal (XTAL) [37]. (b) Total thermal conductivities of three HMS samples plotted in linear scale. (c) Electronic and (d) lattice thermal conductivities of three HMS samples.

The lattice thermal conductivity κ_L is calculated by subtracting the electronic contribution from the total thermal conductivity. The electronic thermal conductivity κ_E in Figure 7(c) is calculated using the Wiedemann-Franz law, $\kappa_E = L\sigma T$, where L is the Lorenz number. It is noted that the constant Lorenz number $L_0 = 2.44 \times 10^{-8} \text{ W } \Omega \text{ K}^{-2}$ failed to accurately represent κ_E when materials deviate from the degenerate limit [68]. Therefore, a corrected Lorenz number for semiconductors, determined based on the measured Seebeck coefficient is used and provided in Supplementary Material. The corrected Lorenz

number for quench-annealed Ru-HMS sample is $1.85 \times 10^{-8} \text{ W } \Omega \text{ K}^{-2}$ at 300 K, significantly smaller than L_0 . With Ru doping, κ_E is suppressed by up to 80% at 22 K. κ_L is calculated using $\kappa_L = \kappa - \kappa_E$, as shown in Figure 7(d). It is noted that the lattice thermal conductivity of the Ru-HMS prepared by SSR remains similar to that of undoped samples. This indicates that enhanced scattering from point defects and lattice distortions by Ru-doping has minimal impact on reducing thermal conductivity. Instead, the reduction of κ is primarily attributed to decreased electronic thermal conductivity, as illustrated in Figure 7(c). After quench-annealing, κ_L is reduced as compared to the other two samples.

3.4 Two-Channel Model Analysis and thermoelectric figure of merit

The quench-annealed sample exhibits a significant suppression of the phonon-related peak in the κ curve, although the peak remains discernible. This behavior is characteristic of a "glass-like" thermal transport regime, commonly observed in disordered crystalline materials where phonon propagation is strongly suppressed due to enhanced scattering events. The resulting monotonic increase in lattice thermal conductivity cannot be explained by a classic phonon transport model. In amorphous or highly disordered materials, diffusons are important heat carriers for which the heat transport is characterized with a diffusivity term instead of MFPs used to describe propagons with longer MFPs than their wavelengths [69]. A two-channel model including the propagon and diffuson contributions to κ has been employed to explain the low κ in materials with disorders and complex structures [37, 70-72]. This model is employed here to study the thermal transport in the quench-annealed Ru-HMS sample.

Accounting for the porosity of the polycrystalline sample, the intrinsic thermal conductivity of the solid without porosity (κ_s) is estimated using the Maxwell-Eucken relation [73, 74]:

$$\kappa_s = \kappa_L \frac{2+f}{2-2f}, \quad (3)$$

where f is the porosity and $f = 1 - \rho/\rho_{single}$, where ρ is the sample density and ρ_{single} is the density of the single crystal. The relative density for the QA sample is about 95% determined by the Archimedes method.

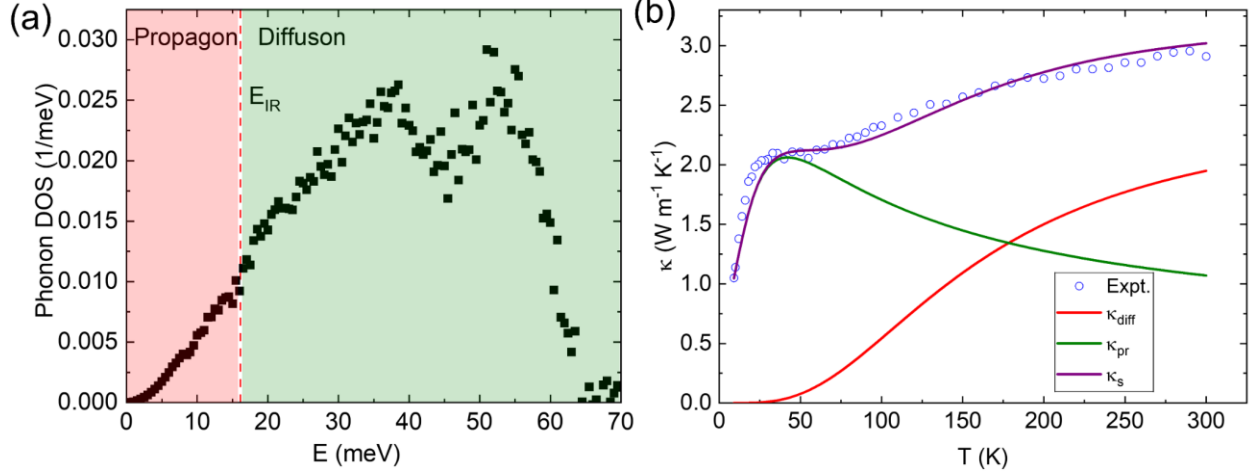


Figure 8. (a) Measured phonon DOS of HMS using inelastic neutron scattering. The data are adapted from [37]. The vertical line indicates the calculated Ioffe-Regel limit. (b) Two-channel model fitting of the lattice thermal conductivity of Ru-HMS sample prepared by melt-quenching followed by annealing.

Based on the two-channel model, $\kappa_s = \kappa_{pr} + \kappa_{diff}$, where κ_{pr} and κ_{diff} represent propagon and diffuson thermal conductivities, respectively. The Ioffe-Regel frequency ω_{IR} corresponding to the Ioffe-Regel limit, where the phonon MFP equals the interatomic spacing, divides the phonon DOS into propagon and diffuson regimes. Below ω_{IR} , lattice thermal transport is described using the Callaway model for propagons, while above ω_{IR} , it is modeled using the random walk theory with thermal diffusivity. In HMS, ω_{IR} is calculated to be 24.5 THz (16 meV), as shown by the red line in Figure 8(a). A detailed analysis of the two-channel model can be found in the Supplementary Material. The two-channel model fitting is shown in Figure 8(b). The fitting successfully reproduces the temperature dependence of lattice thermal conductivity of quench-annealed Ru-HMS. The diffuson contribution to κ starts above 50 K and accounts for approximately 60% of the lattice thermal conductivity at 300 K.

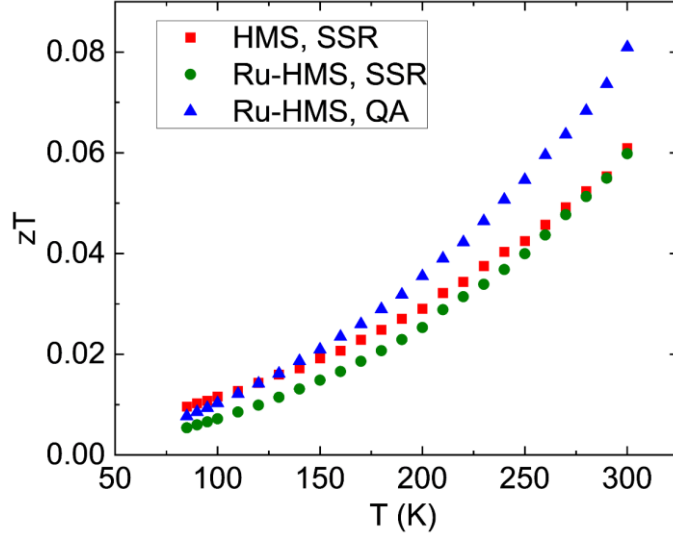


Figure 9. Calculated zT of three HMS samples.

Figure 9 shows the calculated zT of three samples. In the case of quench-annealed Ru-HMS sample, there is a notable increase in zT of about 33% at 300 K compared to the undoped sample. This enhancement can be attributed to several factors. The quench-annealing process increases the carrier concentration, while the Seebeck coefficient remains unaffected due to the effective mass enhancement. As a result, the PF is improved. Furthermore, the lattice thermal conductivity is suppressed due to increased nanostructure scattering. Consequently, the combination of higher PF and lower lattice thermal conductivity leads to a substantial improvement in the overall zT for the quench-annealed sample.

4. Conclusions

This study reports suppressed thermal conductivity and enhanced thermoelectric properties in Ru-doped HMS with grain boundary nanostructures. The melt-quench-annealing process leads to the formation of MnSi nanoprecipitates and pores near the grain boundaries. As a result, the quench-annealed sample exhibits a weak temperature-dependent thermal conductivity, resembling glass-like thermal transport behavior. A two-channel model incorporating contributions from propagons and diffusons is employed to understand this unusual thermal transport. The diffuson contribution to thermal conductivity begins above 50 K and accounts for approximately 60% of lattice thermal conductivity at 300 K. Furthermore, the quench-annealed Ru-HMS exhibits a higher carrier concentration while maintaining a similar Seebeck coefficient compared to the undoped sample, attributed to its increased effective mass of $12 m_0$. The PF of the quench-annealed Ru-HMS is significantly higher than that of the undoped sample. Owing to improved

PF and reduced thermal conductivity, the quench-annealed Ru-HMS sample demonstrates a 33% enhancement in zT at 300 K compared to the undoped sample. These findings demonstrate a promising strategy for tailoring phonon transport through in situ grain boundary engineering, providing valuable insights for the design of high-performance thermoelectric materials.

While our current study focuses on characterizing the TE performance of the resulting materials, we acknowledge that controlling the size and distribution of nanostructures could provide an additional lever to optimize phonon and charge transport. Further studies are needed to understand the effect of synthesis parameters, such as quenching rate, annealing temperature, and dwell time on the microstructure and TE properties of HMS.

CRedit authorship contribution statement

Youming Xu: Writing – review & editing, Writing – original draft, Methodology, Investigation, Data curation. **Shuchen Li:** Writing – review & editing, Investigation, Data curation. **Shucheng Guo:** Writing – review & editing, Methodology, Investigation. **Jianshi Zhou:** Writing – review & editing, Investigation, Supervision. **Li Shi:** Writing – review & editing, Investigation, Supervision, **Xi Chen:** Writing – review & editing, Writing – original draft, Conceptualization, Investigation, Supervision, Funding acquisition.

Declaration of competing interest

The authors declare that they have no known competing financial interests or personal relationships that could have appeared to influence the work reported in this paper.

Acknowledgements

This work was supported by the National Science Foundation under Grant No. 2144328. J. Zhou was supported by NSF MRSEC DMR-2308817.

Data availability

Data will be made available on request.

Supplementary material

Supplementary material associated with this article can be found, in the online version, at XXX.

References

- [1] F. J. DiSalvo, Thermoelectric cooling and power generation, *Science* **285**, 703 (1999).
- [2] B. C. Sales, Thermoelectric materials. Smaller is cooler, *Science* **295**, 1248 (2002).
- [3] T. Zhu, Y. Liu, C. Fu, J. P. Heremans, J. G. Snyder, and X. Zhao, Compromise and Synergy in High-Efficiency Thermoelectric Materials, *Advanced Materials* **29**, 1605884 (2017).
- [4] J. Mao, G. Chen, and Z. Ren, Thermoelectric cooling materials, *Nature Materials* **20**, 454 (2021).
- [5] D. Kraemer *et al.*, High-performance flat-panel solar thermoelectric generators with high thermal concentration, *Nature Materials* **10**, 532 (2011).
- [6] S. Khan, J. Kim, K. Roh, G. Park, and W. Kim, High power density of radiative-cooled compact thermoelectric generator based on body heat harvesting, *Nano Energy* **87**, 106180 (2021).
- [7] H. Wang, Y. Pei, A. D. LaLonde, and G. J. Snyder, Heavily doped p-type PbSe with high thermoelectric performance: an alternative for PbTe, *Advanced Materials* **23**, 1366 (2011).
- [8] R. J. Mehta, Y. Zhang, C. Karthik, B. Singh, R. W. Siegel, T. Borca-Tasciuc, and G. Ramanath, A new class of doped nanobulk high-figure-of-merit thermoelectrics by scalable bottom-up assembly, *Nature materials* **11**, 233 (2012).
- [9] C. Zhou *et al.*, Polycrystalline SnSe with a thermoelectric figure of merit greater than the single crystal, *Nat Mater* **20**, 1378 (2021).
- [10] T. Xing *et al.*, Ultralow lattice thermal conductivity and superhigh thermoelectric figure-of-merit in (Mg, Bi) co-doped GeTe, *Advanced Materials* **33**, 2008773 (2021).
- [11] K. F. Hsu, S. Loo, F. Guo, W. Chen, J. S. Dyck, C. Uher, T. Hogan, E. K. Polychroniadis, and M. G. Kanatzidis, Cubic $\text{AgPb}_{1-x}\text{SbTe}_{2+x}$: Bulk Thermoelectric Materials with High Figure of Merit, *Science* **303**, 818 (2004).
- [12] B. Poudel *et al.*, High-Thermoelectric Performance of Nanostructured Bismuth Antimony Telluride Bulk Alloys, *Science* **320**, 634 (2008).
- [13] T. Mori, Novel Principles and Nanostructuring Methods for Enhanced Thermoelectrics, *Small* **13**, 1702013 (2017).
- [14] J. Ma *et al.*, Glass-like phonon scattering from a spontaneous nanostructure in AgSbTe_2 , *Nature Nanotechnology* **8**, 445 (2013).
- [15] C. B. Vining, A model for the high-temperature transport properties of heavily doped n-type silicon-germanium alloys, *Journal of Applied Physics* **69**, 331 (1991).
- [16] C. Fu, S. Bai, Y. Liu, Y. Tang, L. Chen, X. Zhao, and T. Zhu, Realizing high figure of merit in heavy-band p-type half-Heusler thermoelectric materials, *Nature Communications* **6**, 8144 (2015).

- [17] J. P. Heremans, V. Jovovic, E. S. Toberer, A. Saramat, K. Kurosaki, A. Charoenphakdee, S. Yamanaka, and G. J. Snyder, Enhancement of thermoelectric efficiency in PbTe by distortion of the electronic density of states, *Science* **321**, 554 (2008).
- [18] Y. Pei, X. Shi, A. LaLonde, H. Wang, L. Chen, and G. J. Snyder, Convergence of electronic bands for high performance bulk thermoelectrics, *Nature* **473**, 66 (2011).
- [19] W. Liu, X. Tan, K. Yin, H. Liu, X. Tang, J. Shi, Q. Zhang, and C. Uher, Convergence of Conduction Bands as a Means of Enhancing Thermoelectric Performance of Sn -Type $\text{Mg}_2\text{Si}_x\text{Sn}_{1-x}$ Solid Solutions, *Physical Review Letters* **108**, 166601 (2012).
- [20] S. Han *et al.*, Strong phonon softening and avoided crossing in aliovalence-doped heavy-band thermoelectrics, *Nature Physics* **19**, 1649 (2023).
- [21] W. Kim, Strategies for engineering phonon transport in thermoelectrics, *Journal of Materials Chemistry C* **3**, 10336 (2015).
- [22] H. Liu *et al.*, Copper ion liquid-like thermoelectrics, *Nature Materials* **11**, 422 (2012).
- [23] Y. Xu *et al.*, Crystal Structure and Thermoelectric Properties of Layered Van der Waals Semimetal ZrTiSe_4 , *Chemistry of Materials* **34**, 8858 (2022).
- [24] Z.-H. Ge, L.-D. Zhao, D. Wu, X. Liu, B.-P. Zhang, J.-F. Li, and J. He, Low-cost, abundant binary sulfides as promising thermoelectric materials, *Materials Today* **19**, 227 (2016).
- [25] K. Suekuni, K. Tsuruta, M. Kunii, H. Nishiate, E. Nishibori, S. Maki, M. Ohta, A. Yamamoto, and M. Koyano, High-performance thermoelectric mineral $\text{Cu}_{12-x}\text{Ni}_x\text{Sb}_4\text{S}_{13}$ tetrahedrite, *Journal of Applied Physics* **113** (2013).
- [26] M. Acharya, S. S. Jana, M. Ranjan, and T. Maiti, High performance ($\text{ZT} > 1$) n-type oxide thermoelectric composites from earth abundant materials, *Nano Energy* **84**, 105905 (2021).
- [27] T. Barbier, S. Rollin-Martinet, P. Lemoine, F. Gascoin, A. Kaltzoglou, P. Vaqueiro, A. V. Powell, and E. Guilmeau, Thermoelectric Materials: A New Rapid Synthesis Process for Nontoxic and High-Performance Tetrahedrite Compounds, *Journal of the American Ceramic Society* **99**, 51 (2016).
- [28] O. Schwomma, A. Preisinger, H. Nowotny, and A. Wittmann, Die Kristallstruktur von $\text{Mn}_{11}\text{Si}_{19}$ und deren Zusammenhang mit Disilicid-Typen, *Monatshefte für Chemie und verwandte Teile anderer Wissenschaften* **95**, 1527 (1964).
- [29] H. Nowotny, *The Chemistry of Extended Defects in Non-Metallic Solids*, North-Holland Publishing Co. Amsterdam (1970).
- [30] H. W. Knott, M. H. Mueller, and L. Heaton, The crystal structure of $\text{Mn}_{15}\text{Si}_{26}$, *Acta Crystallographica* **23**, 549 (1967).
- [31] G. Zwillling and H. Nowotny, Zur Struktur der Defekt-Mangansilicide Kristallstruktur von $\text{Mn}_{27}\text{Si}_{47}$, *Monatshefte für Chemie* **104**, 668 (1973).
- [32] W.-D. Liu, Z.-G. Chen, and J. Zou, Eco-Friendly Higher Manganese Silicide Thermoelectric Materials: Progress and Future Challenges, *Advanced Energy Materials* **8**, 1800056 (2018).

- [33] S. Muthiah, R. C. Singh, B. D. Pathak, P. K. Avasthi, R. Kumar, A. Kumar, A. K. Srivastava, and A. Dhar, Significant enhancement in thermoelectric performance of nanostructured higher manganese silicides synthesized employing a melt spinning technique, *Nanoscale* **10**, 1970 (2018).
- [34] W. Luo, H. Li, Y. Yan, Z. Lin, X. Tang, Q. Zhang, and C. Uher, Rapid synthesis of high thermoelectric performance higher manganese silicide with in-situ formed nano-phase of MnSi, *Intermetallics* **19**, 404 (2011).
- [35] D. Y. Nhi Truong, H. Kleinke, and F. Gascoin, Preparation of pure Higher Manganese Silicides through wet ball milling and reactive sintering with enhanced thermoelectric properties, *Intermetallics* **66**, 127 (2015).
- [36] Z. Li *et al.*, MnS Incorporation into Higher Manganese Silicide Yields a Green Thermoelectric Composite with High Performance/Price Ratio, *Advanced Science* **5**, 1800626 (2018).
- [37] X. Chen *et al.*, Twisting phonons in complex crystals with quasi-one-dimensional substructures, *Nat Commun* **6**, 6723 (2015).
- [38] X. Chen, S. N. Girard, F. Meng, E. Lara-Curzio, S. Jin, J. B. Goodenough, J. Zhou, and L. Shi, Approaching the Minimum Thermal Conductivity in Rhenium-Substituted Higher Manganese Silicides, *Advanced Energy Materials* **4**, 1400452 (2014).
- [39] A. J. Zhou, X. B. Zhao, T. J. Zhu, S. H. Yang, T. Dasgupta, C. Stiewe, R. Hassdorf, and E. Mueller, Microstructure and thermoelectric properties of SiGe-added higher manganese silicides, *Materials Chemistry and Physics* **124**, 1001 (2010).
- [40] W. Luo, H. Li, F. Fu, W. Hao, and X. Tang, Improved Thermoelectric Properties of Al-Doped Higher Manganese Silicide Prepared by a Rapid Solidification Method, *Journal of Electronic Materials* **40**, 1233 (2011).
- [41] N. S. Chauhan, I. Ono, and Y. Miyazaki, Lattice anharmonicity in charge compensated higher manganese silicide single crystals, *Journal of Materials Chemistry A* **11**, 19107 (2023).
- [42] L. Xu *et al.*, Exploiting synergies for high thermoelectric performance in higher manganese silicide-based semiconductors through element Co-doping, energy filtering, and phonon scattering, *Ceramics International* **50**, 17604 (2024).
- [43] H. Mun, S.-M. Choi, K. H. Lee, and S. W. Kim, Boundary Engineering for the Thermoelectric Performance of Bulk Alloys Based on Bismuth Telluride, *ChemSusChem* **8**, 2312 (2015).
- [44] Q. Zhang *et al.*, Realizing high-performance thermoelectric power generation through grain boundary engineering of skutterudite-based nanocomposites, *Nano Energy* **41**, 501 (2017).
- [45] S. I. Kim *et al.*, Dense dislocation arrays embedded in grain boundaries for high-performance bulk thermoelectrics, *Science* **348**, 109 (2015).
- [46] J. Lei *et al.*, Approaching crystal's limit of thermoelectrics by nano-sintering-aid at grain boundaries, *Nature Communications* **15**, 6588 (2024).

- [47] P. He and Y. Wu, Constructing of highly porous thermoelectric structures with improved thermoelectric performance, *Nano Research* **14**, 3608 (2021).
- [48] B. Xu, T. Feng, M. T. Agne, L. Zhou, X. Ruan, G. J. Snyder, and Y. Wu, Highly porous thermoelectric nanocomposites with low thermal conductivity and high figure of merit from large-scale solution-synthesized Bi_2Te_3 hollow nanostructures, *Angewandte Chemie International Edition* **56**, 3546 (2017).
- [49] H.-L. Zhuang, H. Hu, J. Pei, B. Su, J.-W. Li, Y. Jiang, Z. Han, and J.-F. Li, High ZT in p-type thermoelectric $(\text{Bi}, \text{Sb})_2\text{Te}_3$ with built-in nanopores, *Energy & Environmental Science* **15**, 2039 (2022).
- [50] X. Shi, A. Wu, W. Liu, R. Moshwan, Y. Wang, Z.-G. Chen, and J. Zou, Polycrystalline SnSe with extraordinary thermoelectric property via nanoporous design, *ACS nano* **12**, 11417 (2018).
- [51] K.-H. Lee *et al.*, Enhancement of Thermoelectric Figure of Merit for $\text{Bi}_0.5\text{Sb}_{1.5}\text{Te}_3$ by Metal Nanoparticle Decoration, *Journal of Electronic Materials* **41**, 1165 (2012).
- [52] X. Meng *et al.*, Grain Boundary Engineering for Achieving High Thermoelectric Performance in n-Type Skutterudites, *Advanced Energy Materials* **7**, 1602582 (2017).
- [53] X. Chen, A. Weathers, A. Moore, J. Zhou, and L. Shi, Thermoelectric Properties of Cold-Pressed Higher Manganese Silicides for Waste Heat Recovery, *Journal of Electronic Materials* **41**, 1564 (2012).
- [54] F. Tian *et al.*, Unusual high thermal conductivity in boron arsenide bulk crystals, *Science* **361**, 582 (2018).
- [55] X. Chen, J. Carrete, S. Sullivan, A. van Roekeghem, Z. Y. Li, X. Li, J. S. Zhou, N. Mingo, and L. Shi, Coupling of Spinons with Defects and Phonons in the Spin Chain compound Ca_2CuO_3 , *Physical Review Letters* **122** (2019).
- [56] S. Wang, H. Li, D. Qi, W. Xie, and X. Tang, Enhancement of the thermoelectric performance of $\beta\text{-Zn}_4\text{Sb}_3$ by in situ nanostructures and minute Cd-doping, *Acta Materialia* **59**, 4805 (2011).
- [57] Y. Jin, Y. Xiao, D. Wang, Z. Huang, Y. Qiu, and L.-D. Zhao, Realizing High Thermoelectric Performance in GeTe through Optimizing Ge Vacancies and Manipulating Ge Precipitates, *ACS Applied Energy Materials* **2**, 7594 (2019).
- [58] W. G. Zeier, A. LaLonde, Z. M. Gibbs, C. P. Heinrich, M. Panthöfer, G. J. Snyder, and W. Tremel, Influence of a Nano Phase Segregation on the Thermoelectric Properties of the p-Type Doped Stannite Compound $\text{Cu}_{2+x}\text{Zn}_{1-x}\text{GeSe}_4$, *Journal of the American Chemical Society* **134**, 7147 (2012).
- [59] H. Strandlund and H. Larsson, Prediction of Kirkendall shift and porosity in binary and ternary diffusion couples, *Acta Materialia* **52**, 4695 (2004).
- [60] V. Ponnambalam, D. T. Morelli, S. Bhattacharya, and T. M. Tritt, The role of simultaneous substitution of Cr and Ru on the thermoelectric properties of defect manganese silicides MnSi_δ ($1.73 < \delta < 1.75$), *Journal of alloys and compounds* **580**, 598 (2013).

- [61] M. Cutler and N. F. Mott, Observation of Anderson localization in an electron gas, *Physical Review* **181**, 1336 (1969).
- [62] X. Chen, J. Zhou, J. B. Goodenough, and L. Shi, Enhanced thermoelectric power factor of Re-substituted higher manganese silicides with small islands of MnSi secondary phase, *Journal of Materials Chemistry C* **3**, 10500 (2015).
- [63] S. N. Girard, X. Chen, F. Meng, A. Pokhrel, J. Zhou, L. Shi, and S. Jin, Thermoelectric properties of undoped high purity higher manganese silicides grown by chemical vapor transport, *Chemistry of Materials* **26**, 5097 (2014).
- [64] X. Chen, A. Weathers, D. Salta, L. Zhang, J. Zhou, J. B. Goodenough, and L. Shi, Effects of (Al,Ge) double doping on the thermoelectric properties of higher manganese silicides, *Journal of Applied Physics* **114**, 173705 (2013).
- [65] X. She, X. Su, H. Du, T. Liang, G. Zheng, Y. Yan, R. Akram, C. Uher, and X. Tang, High thermoelectric performance of higher manganese silicides prepared by ultra-fast thermal explosion, *Journal of Materials Chemistry C* **3**, 12116 (2015).
- [66] Q. Guo *et al.*, Thermoelectric performance of Cr doped and Cr–Fe double-doped higher manganese silicides with adjusted carrier concentration and significant electron–phonon interaction, *ACS Applied Materials & Interfaces* **13**, 8574 (2021).
- [67] Y. Li, H. Y. Bai, W. H. Wang, and K. Samwer, Low-temperature specific-heat anomalies associated with the boson peak in CuZr-based bulk metallic glasses, *Physical Review B* **74**, 052201 (2006).
- [68] H.-S. Kim, Z. M. Gibbs, Y. Tang, H. Wang, and G. J. Snyder, Characterization of Lorenz number with Seebeck coefficient measurement, *APL Materials* **3** (2015).
- [69] M. T. Agne, R. Hanus, and G. J. Snyder, Minimum thermal conductivity in the context of diffuson-mediated thermal transport, *Energy & Environmental Science* **11**, 609 (2018).
- [70] T. Bernges, M. Peterlechner, G. Wilde, M. T. Agne, and W. G. Zeier, Analytical model for two-channel phonon transport engineering, *Materials Today Physics* **35**, 101107 (2023).
- [71] Y. Xu, Y. Wu, H. Cao, S. Guo, J. Yan, and X. Chen, Single crystal growth and thermoelectric properties of Nowotny chimney-ladder compound Fe₂Ge₃, *Physical Review Materials* **7**, 125404 (2023).
- [72] Y. Wang *et al.*, Origin of Intrinsically Low Thermal Conductivity in a Garnet-Type Solid Electrolyte: Linking Lattice and Ionic Dynamics with Thermal Transport, *PRX Energy* **4**, 033004 (2025).
- [73] D. S. Smith *et al.*, Thermal conductivity of porous materials, *Journal of Materials Research* **28**, 2260 (2013).
- [74] S. Guo, H. Li, X. Bai, Y. Wang, S. Li, R. E. Dunin-Borkowski, J. Zhou, and X. Chen, Size-dependent magnon thermal transport in a nanostructured quantum magnet, *Cell Reports Physical Science* **5** (2024).

